NANO LETTERS

pubs.acs.org/NanoLett

Mini-Review

Black Phosphorus for Mid-Infrared Optoelectronics: Photophysics, Scalable Processing, and Device Applications

Naoki Higashitarumizu, Shu Wang, Shifan Wang, Hyungjin Kim, James Bullock, and Ali Javey*

Cite This: *Nano Lett.* 2024, 24, 13107−13117

Read Online

ACCESS | Metrics & More | Article Recommendations

ABSTRACT: High efficiency mid-infrared (λ = 3−8 μm) light emitters and photodetectors are pivotal for advancing next-generation optoelectronics. However, narrow-bandgap semiconductors face fundamental challenges such as pronounced nonradiative carrier recombination and thermally generated noise, which impede device performance. Recently, two-dimensional layered black phosphorus (BP) and its alloys have attracted substantial interest for mid-infrared device applications, demonstrating superior performance relative to conventional III−V and II−VI semiconductors with similar bandgaps. In this review, we discuss the optical properties of BP, contrasting these with those of covalent compounds. Owing to its inherently self-terminated surface structure and reduced nonradiative recombination, BP exhibits high performance in light emission and photodetection at room temperature. Furthermore, this review highlights recent advances in the large-area processing of BP thin films, paving the way for practical device applications and integration. Finally, we explore ongoing challenges and emerging opportunities in the utilization of BP for functional mid-infrared devices.

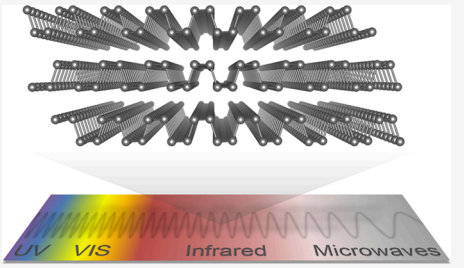

KEYWORDS: *mid-infrared, black phosphorus, light emitters, photodetectors, thin film process*

Downloaded via UNIV OF CALIFORNIA BERKELEY on January 14, 2025 at 19:52:09 (UTC).
See https://pubs.acs.org/sharingguidelines for options on how to legitimately share published articles.

Highly efficient optoelectronics in the mid-infrared (mid-IR, λ = 3−8 μm, Figure 1a) have become increasingly important for pioneering next-generation technologies, including gas sensing,[1,2] spectroscopy,[3] noninvasive biomedical imaging,[4−6] thermal imaging,[7−9] and thermal photovoltaic applications[10,11] (Figure 1b−d). The mid-IR wavelength covers the light absorption bands of various gases and biomolecules and corresponds to a broad spectrum of thermal radiation, delivering useful information for medical, defense, industrial, infrastructure, and building maintenance applications. The advancement of mid-IR light emitters and photodetectors requires addressing key challenges like nonradiative recombination and thermal noise, which are prominent in materials with narrow bandgaps.[12] Nonradiative recombination processes such as Auger and surface recombination significantly curtail the luminescence efficiency in thin active layers. Additionally, thermally generated current noise is significant in photodetectors with narrow-bandgap materials, making highly sensitive mid-IR sensors feasible only when cooled, which increases the size, weight, power, and cost (SWaP-C) characteristics of the detectors. As such, a materials-based breakthrough is essential to realize compact, power-efficient, and cost-effective mid-IR optoelectronic devices.

Multilayer black phosphorus (BP), with its narrow bandgap and layered structure, has rapidly established itself as a promising building block for mid-IR optoelectronics,[12−20] along with interests in its electronic properties such as high carrier mobility.[21−23] BP's unique band structure and inherently self-terminated crystal structure contribute to optoelectronic performance that surpass those of conventional III−V and II−VI semiconductors with similar bandgaps, such as HgCdTe, InSb, and PbS.[12−16] BP-based mid-IR light-emitting diodes (LEDs) have achieved an external quantum efficiency (EQE) as high as 4.4%, outperforming commercially available mid-IR LEDs (EQE = 0.1−0.9%).[15−17] Moreover, BP-based photodetectors have demonstrated exceptional specific detectivities (D^*) of (1−6) × 10^{10} cm $Hz^{1/2}$ W^{-1} at room temperature (RT), comparable to uncooled HgCdTe detectors ($D^* \approx 10^{10}$ cm $Hz^{1/2}$ W^{-1}).[13,14] Beyond its superior light emission and detection properties, BP offers functional benefits, including bandgap tunability, polarized optical properties, and compatibility with various material and device platforms. This mini-review summarizes recent progress in mid-IR light emitters and photodetectors employing BP, comparing these to conventional covalently bonded compound semiconductors. While initial studies primarily utilized mechanically exfoliated BP flakes at the micrometer scale for basic optical property exploration and proof-of-concept device demonstrations, we also review recent progress in large-scale thin film processing toward practical device applications. We

Received: August 19, 2024
Revised: October 11, 2024
Accepted: October 11, 2024
Published: October 15, 2024

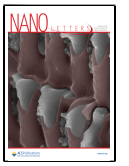

ACS Publications

© 2024 American Chemical Society

https://doi.org/10.1021/acs.nanolett.4c04027
Nano Lett. 2024, 24, 13107−13117

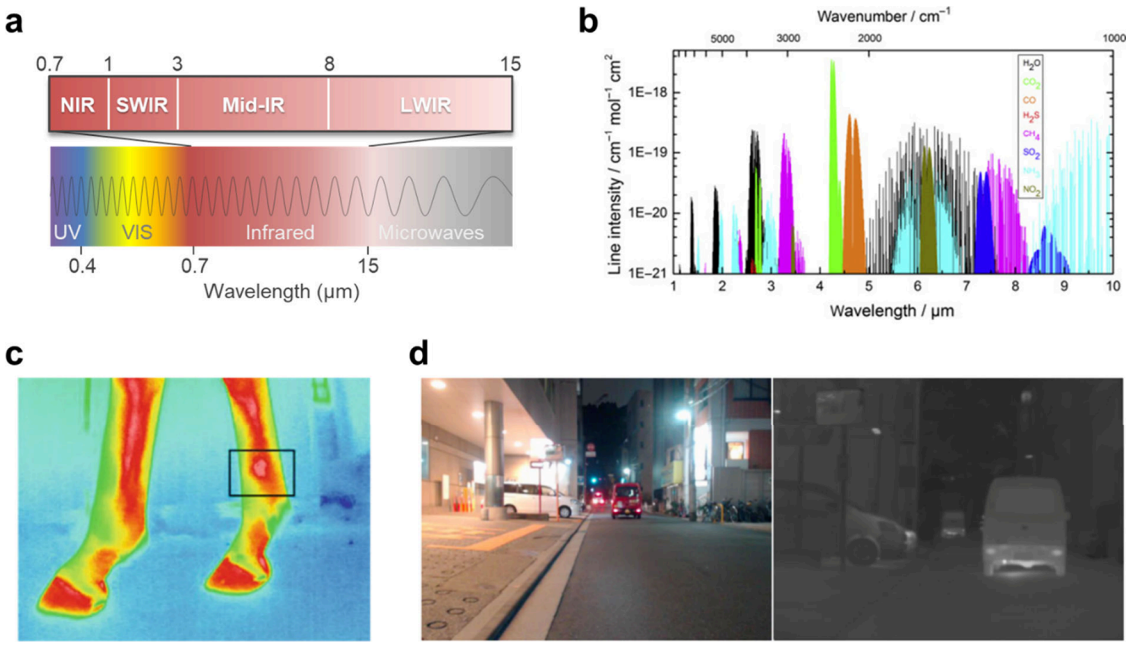

Figure 1. Mid-IR optoelectronic applications. (a) Wavelength diagram of ultraviolet (UV), visible (VIS), near-IR (NIR), shortwave-IR (SWIR), mid-IR, and longwave-IR (LWIR). (b) Light absorption spectra of various gas molecules. Reprinted with permission from ref 1. Copyright 2020 Elsevier Ltd. (c) A thermal image visualizing inflammation in the leg of a horse, as marked with a box. Reproduced with permission from ref 6. Copyright 2014 Springer Nature. (d) Automotive thermal imaging camera: visible light imaging with RGB three-channel (left) and thermal imaging (right). Reproduced with permission from ref 9. Copyright 2020 SPIE.

conclude with a perspective on future research directions that could further advance mid-IR optoelectronics.

PHOTOPHYSICS IN BLACK PHOSPHORUS

Figure 2a illustrates the crystal structure of multilayer BP in the ground state of the orthorhombic phase, where each phosphorus atom forms covalent bonds with two others in each layer. Figure 2b,c shows a typical cross-sectional high-resolution transmission electron microscope (TEM) image of bulk BP along the armchair direction and the fast Fourier transform (FFT) pattern image.[24] This puckered structure along the armchair direction (x) gives rise to in-plane anisotropic optical and electrical transport properties.[21] BP maintains a direct bandgap across all thicknesses from monolayer to bulk,[12] unlike other layered materials such as transition-metal dichalcogenides (TMDs: e.g., MoS_2, WS_2) which undergoes a direct-to-indirect the bandgap transition from a monolayer to multilayers.[25,26] In the TMD monolayers, enhanced Coulomb interaction enables the neutral excitons to be bright at RT, even with a high density of native defects. The photoluminescence (PL) quantum yield (QY), a key metric of optoelectronic performance, can be near unity in the TMD monolayers with optimal chemical or electrostatic counter-doping.[27−29] The monolayer materials are of interest for their optical properties, though there is a fundamental limitation in light output power and light interactions due to their ultimately thin thickness compared to the wavelength of light, potentially constraining device performance. Consequently, the direct bandgap state of bulk BP facilitates the development of highly efficient optical devices beyond the monolayer limits. Figure 2d shows the simulated band structure of bulk BP through density functional theory (DFT) calculations with different methods, indicating a narrow direct bandgap at the Z point in the range 0.31−0.36 eV,[22] consistent with the experimental optical bandgap of 0.31−0.35 eV, corresponding to mid-IR wavelengths (λ = 3.5−4.0 μm).[12,14,19,20] The band structure of a monolayer is also shown in Figure 2d, indicating the direct bandgap of 1.41−1.51 eV obtained at the G point.[22] As shown in Figure 2e, BP's PL spectrum peak position varies widely from 0.32 eV in bulk to 1.67 eV in monolayer form. As the thickness of BP decreases to a few-to-monolayers, carrier recombination transitions from a free-carrier to an excitonic system due to reduced Coulomb screening.[12,30] Few-to-monolayer BP exhibits excitonic emissions, while at a thickness above five layers, the exciton binding energy is similar to or lower than the thermal energy at RT,[12] making the free-carrier band-to-band transition dominant (Figure 2f). For BP layers exceeding ten layers, the luminescence wavelength resembles that of bulk BP. Given that the absorption coefficient of BP is approximately 10^4 cm^{-1} from its band edge to near-IR wavelength,[14] most reasonable photodetection applications in the mid-IR generally require thicknesses greater than 10 nm, considered as bulk BP in this paper.

In conventional semiconductors, nonequilibrium populations of electrons and holes relax mainly through four different pathways: bulk and surface Shockley−Read−Hall (SRH),[31−33] bimolecular radiative, and Auger[34] recombination. The bulk and surface SRH recombinations are nonradiative carrier recombination at trap states inside the bulk and at the surface of the active layer, respectively, while Auger recombination is a nonradiative process involving three carriers where the energy is given to a third carrier excited to a higher level instead of generating light (Figure 2f). The PL QY determines the maximum device radiative efficiency. According to a standard ABC recombination model, QY can be written as

https://doi.org/10.1021/acs.nanolett.4c04027
Nano Lett. 2024, 24, 13107−13117

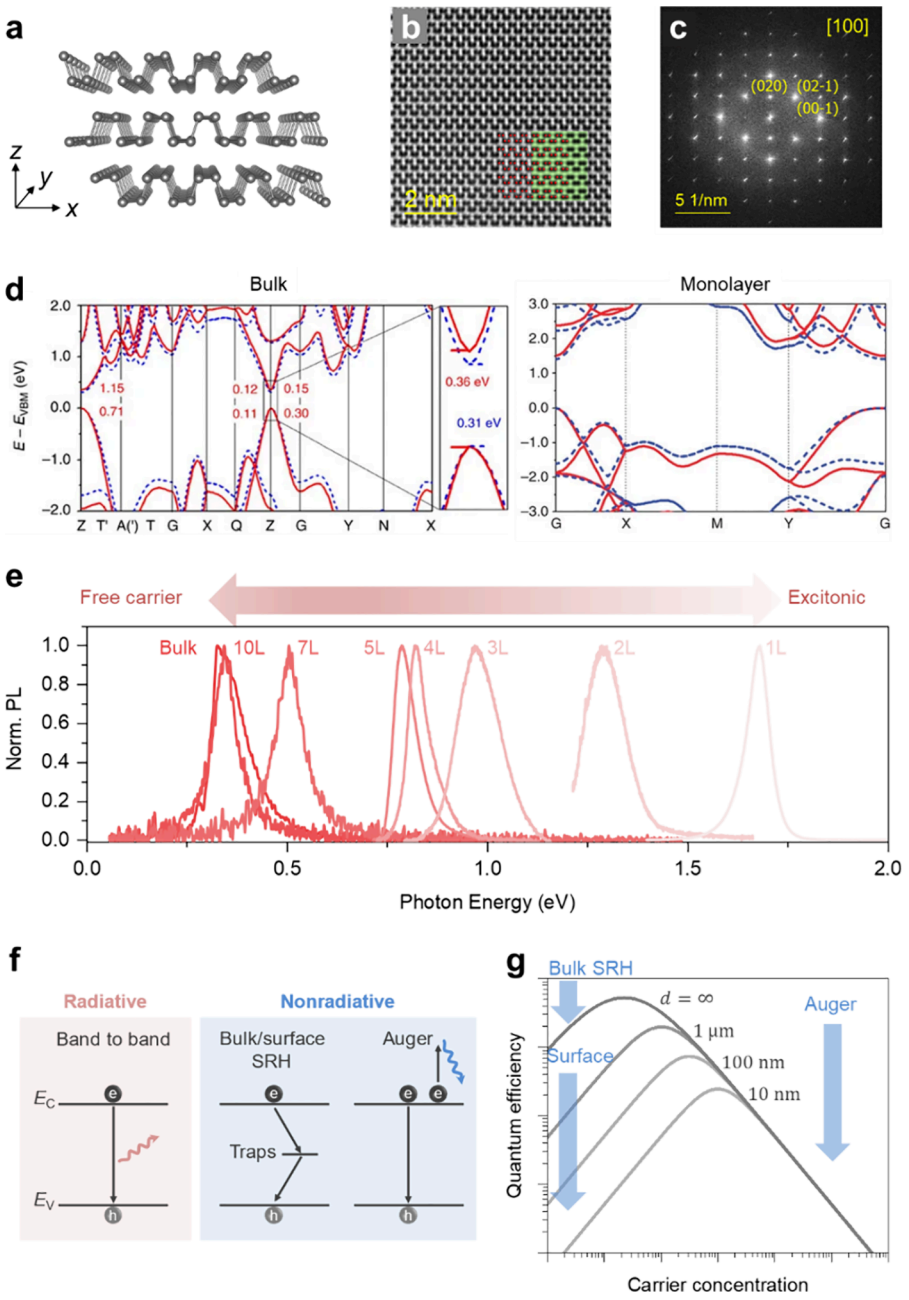

Figure 2. Optical properties of bulk BP. (a) Crystal structure of bulk BP. (b) Cross sectional high-resolution TEM image and (c) FFT pattern image of BP. Inset: atomic model along the armchair direction shown in red and a simulated high-resolution TEM image marked with a green box. Reproduced (adapted) with permission from ref 24. Copyright 2018 IOP Publishing, Ltd. (d) Electronic band structures of bulk and monolayer BP calculated by density functional theory, with the HSE06 functional (red solid line) and the mBJ potential (blue dashed line). Reproduced (adapted) with permission from ref 22. Copyright 2014 Springer Nature. (e) Normalized PL spectra of BP with different thickness from bulk to monolayer, where carrier recombination changes from a free carrier to excitonic system. Reproduced (adapted) with permission from ref 12. Copyright 2023 Springer Nature. (f) Radiative and nonradiative free carrier recombination processes in bulk BP. (g) Log−log plot of the quantum efficiency versus carrier concentration with different active layer thicknesses of 10 nm, 100 nm, 1 μm, and infinite thickness. Bulk and surface SRH recombinations are predominant at low injection carrier concentration, while Auger recombination limits quantum efficiency under high injection carrier concentration.

$$\mathrm{QY} = \frac{B(n^2 - n_i^2)}{(A + 2S/d)\frac{n^2 - n_i^2}{n} + B(n^2 - n_i^2) + Cn(n^2 - n_i^2)} \quad (1)$$

where A, B, and C are bulk SRH, radiative, and Auger recombination rates, S is surface recombination velocity, n is carrier concentration, n_i is the intrinsic carrier concentration, and d is the active layer. At low carrier concentration, bulk and surface SRH recombinations contribute to decreased quantum efficiency, limiting photodetection; at high carrier concentration, Auger recombination dominates the decrease in quantum efficiency, mainly preventing bright light emission (Figure 2g). Notably, surface recombination significantly reduces the QY when the active layer becomes thinner. These trends have been observed in bulk BP through quantitative PL QY measurements as a function of generation

https://doi.org/10.1021/acs.nanolett.4c04027
Nano Lett. 2024, 24, 13107−13117

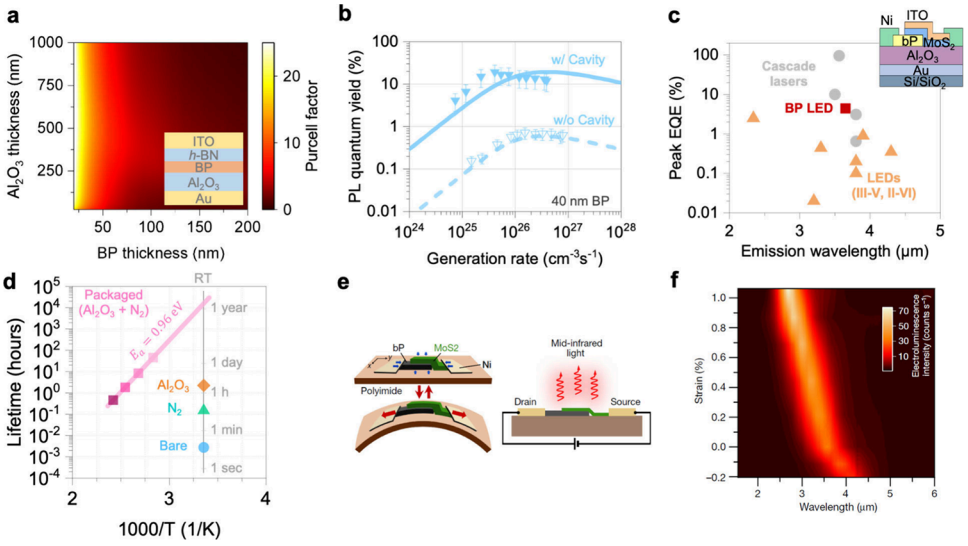

Figure 3. BP-based mid-IR emitters. (a) FDTD simulation result of Purcell factor in bulk BP as a function of Al_2O_3 and BP thicknesses. ITO and *h*-BN thicknesses were fixed at 50 and 30 nm, respectively. Inset: schematic view of BP with optical cavity, ITO/*h*-BN/BP/Al_2O_3/Au structure. Reproduced with permission from ref 12. Copyright 2023 Springer Nature. (b) The generation rate-dependent PL QY of 40 nm BP in an optical cavity in comparison with the BP on a 50 nm SiO_2/Si substrate. Solid and dashed lines represent the ABC model fitting for BP in a cavity and BP on a SiO_2/Si substrate, respectively. Reproduced with permission from ref 12. Copyright 2023 Springer Nature. (c) Benchmark comparison of peak EQE for BP-LED with peak EQEs reported for various published and commercial infrared light sources at room temperature. The inset illustrates the device structure of BP-LED based on a BP/MoS_2 heterojunction. Reproduced (adapted) with permission from ref 16. Copyright 2022 American Chemical Society. (d) Lifetime of BP-LED with different conditions: bare, N_2 atmosphere, Al_2O_3 passivation, and packaged (N_2 sealing + Al_2O_3 passivation), as a function of inverse temperature (T^{-1}). The room-temperature lifetime of packaged BP-LEDs is estimated from the solid line fit to the lifetimes measured at elevated temperatures. Reproduced with permission from ref 17. Copyright 2023 Springer Nature. (e) Schematic view of a variable-spectrum BP-LED for active tuning of emission wavelength upon external strain application by bending of the substrate. Reproduced with permission from ref 15. Copyright 2021 Springer Nature. (f) Electroluminescence spectra of BP-LED as a function of applied strain in BP. Reproduced with permission from ref 15. Copyright 2021 Springer Nature.

rate and BP thickness.[12] Although preliminary, a few works have reported radiative recombination rates of $B = (2-6) \times 10^{-10}$ cm^3 s^{-1}, which are comparable to those of other narrow-bandgap semiconductors, measured by transient microwave conductivity, transient photocurrent, or time-resolved differential transmission.[35−37] Despite a moderate radiative rate, bulk BP has been shown to be radiatively dominant, exhibiting bright photoluminescence:[12,15,16,19,35] bulk BP's PL QY reaches 2%, and BP-based LEDs show an EQE of 4.4%, exceeding conventional semiconductors with similar bandgaps.[16] This outstanding optical performance can be attributed to suppressed nonradiative recombination effects. The Auger recombination rate in bulk BP has been investigated using transient microwave conductivity measurements, suggesting an unusually low Auger recombination rate compared to other narrow-bandgap semiconductors ($C = 10^{-24}-10^{-28}$ cm^6 s^{-1}).[35] Note that BP's Auger recombination rate was estimated at a specific generation rate of $G = 2.5 \times 10^{25}$ cm^{-3} s^{-1}, meaning that measurement error could be large and further validation is required especially under higher excitation where the Auger effect is more severe.[35] Considering the simplifications and errors in estimating nonradiative rates experimentally, detailed time-resolved and pump-power-dependent luminescence measurements are required to attain a better understanding of BP's nonradiative recombination.

In covalently bonded semiconductor thin films, light emission and photodetection can be limited by nonradiative surface recombination caused by carrier trapping at surface defects, including impurities and dangling bonds.[33] Owing to BP's inherently self-terminated layered structure, surface recombination is suppressed, enabling BP to serve as a highly efficient active layer for light emission and detection.[12,14] Although the BP surface is easily oxidized in air so that defects and native oxides can exist,[38−42] the surface oxidation has a minimal effect on the PL QY in relatively thick BP due to the self-limited oxide formation leaving steep interface with less dangling bonds.[12] Based on DFT calculations, oxygen defect states do not form electronic states within the bandgap, meaning they have less effect on the surface recombination velocity even with surface oxidation.[12,43] In fact, PL stability tests against oxidation have revealed that thin BP layers below ~12 nm show PL QY degradation after air exposure for 1 week; however, relatively thick BP (>50 nm) shows no degradation in optical performance after air exposure for 1 week or even after the harsh oxidation process of oxygen plasma.[12] These results indicate the feasibility of maintaining optical quality in relatively thick BP, suggesting its potential in practical optoelectronic applications.

BRIGHT, ROBUST, AND COLOR-TUNABLE MID-IR EMITTERS

Unlike covalent semiconductors, the integration of BP with an external optical cavity structure does not involve any undesirable effects or stringent requirements owing to its naturally passivated surface without considering lattice matching or temperature compatibilities. As illustrated in Figure 3a, the multilayer cavity structure of BP has been fabricated by inserting BP between top and bottom mirrors and insulating layers. The thickness of Al_2O_3 is controlled to maximize the Purcell factor for BP at a given thickness, and *h*-BN is transferred onto BP as a top insulating layer. Consequently, this optical cavity structure further enhances

https://doi.org/10.1021/acs.nanolett.4c04027
Nano Lett. 2024, 24, 13107−13117

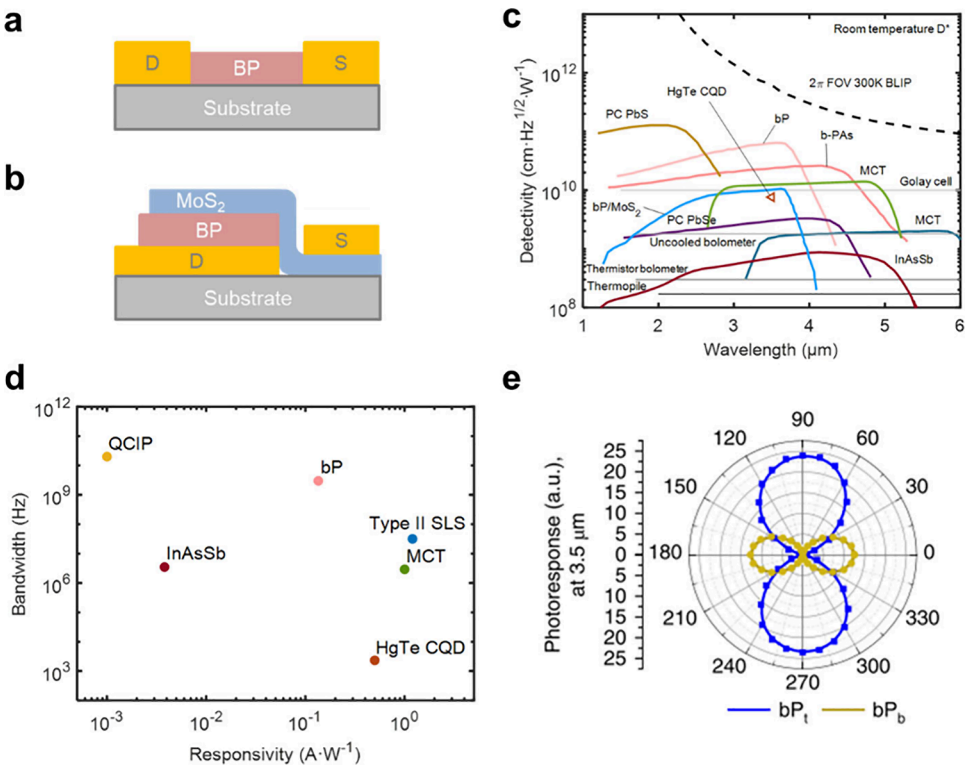

Figure 4. BP-based mid-IR photodetectors. (a,b) Device structure of photoconductors and *p*-*n* heterojunctions made of BP and MoS_2, respectively. S/D denotes the source/drain. (c,d) Benchmarking versus conventional mid-IR detectors: (c) room temperature specific detectivity and (d) response speed (note: PC, photoconductor; BLIP, background-limited performance; CQD, colloidal quantum dots; QCIP, quantum cascading infrared photodetectors, Type II SLS, type II superlattice). Reproduced with permission from ref 80. Copyright 2021 MDPI. (e) Anisotropic photoresponse of a BP/MoS_2/BP measured at λ = 3.5 μm, showing polarization dependent photoresponse, along armchair and zigzag directions. Reproduced with permission from ref 14. Copyright 2018 Springer Nature.

the PL QY of BP reaching up to ~20% at RT for 40 nm BP, exhibiting more than a 10-fold enhancement compared to the PL QY of BP on a 50 nm SiO_2/Si substrate, as shown in Figure 3b.[12]

Commonly used mid-IR light sources are based on thermal emitters, which suffer from poor efficiency, broad spectral width, and a low modulation bandwidth. Although quantum cascade lasers (QCLs) and interband cascade lasers (ICLs) offer narrow-band emission and high brightness, their fabrication complexity, high cost, and high power consumption have limited widespread usage as light sources in this wavelength range.[44,45] LEDs based on III−V and II−VI semiconductors have emerged as alternatives to QCLs/ICLs with their low operating power and fabrication cost, but they have an intrinsic drawback of low EQE, associated with their Auger-dominated carrier recombination.[46,47] Therefore, the high PL QY in BP can be leveraged to develop an LED with high efficiency and overcome the performance bottleneck limiting current mid-IR emitters.

Figure 3c shows the benchmark comparison of the peak EQE of the BP-based LED with other reported various mid-IR emitters, including QCLs/ICLs as well as LEDs based on III−V and II−VI semiconductors.[16,48−55] The device structure of the characterized BP-based LED, described in the inset of Figure 3c, consists of a BP/MoS_2 van der Waals (vdW) heterojunction with *p*-type and *n*-type characteristics, respectively. To reduce the parasitic resistance of MoS_2, an indium tin oxide (ITO) layer is employed as an IR-transparent top electrode, and an Al_2O_3/Au optical cavity structure is adopted to enhance the light outcoupling and Purcell factor, achieving a peak EQE of ~4.4% at an emission wavelength of λ = 3.65 μm. Despite its EQE being lower than those from highly efficient QCLs, the BP-based LED outperforms other state-of-the-art mid-IR light sources in terms of peak EQE measured at RT. Additionally, there is still room for further advances in performance by implementing additional approaches, such as doping and nano-optics.

Major obstacles hindering the practical application of BP for commercial LEDs include instability, where the substantial degradation of its optoelectronic quality is inevitable due to oxidation under more severe carrier injection conditions rather than optical pumping in PL measurements. To address this challenge, a method combining nitrogen (N_2) sealing with Al_2O_3 passivation is proposed to prolong the operating lifetime of the BP-based LED.[17] The lifetimes of the BP-LEDs under different conditions, defined as the operation times required for the EL intensity to reduce to 50% of its starting value, are characterized and plotted in Figure 3d. For accelerated life testing, the operating lifetime of the packaged (N_2 and Al_2O_3) BP-LED was measured at 90, 100, 120, and 140 °C, then the RT lifetime was extrapolated according to the equation

$$t_{L/L_0} = A\left[\ln\left(\frac{L}{L_0}\right)^{-1}\right]^{1/\beta} \exp\left(\frac{E_a}{kT}\right) \quad (2)$$

where L/L_0 is the normalized luminescence, the fitting parameters A and β are determined to be 6.6 × 10^{11} and 0.6, respectively, the activation energy E_a is determined to be 0.96 eV, and k is the Boltzmann constant. The half-lifetime

https://doi.org/10.1021/acs.nanolett.4c04027
Nano Lett. 2024, 24, 13107−13117

($t_{0.5}$) of the packaged BP-LED at RT is then estimated as ~15000 h, suggesting the promising potential of BP-LEDs to attain both high efficiency and environmental stability with a simple and scalable packaging strategy.

BP's optical bandgap is also highly sensitive to strain, which can be exploited to develop a tunable light source based on strained BP.[56,57] Schematics illustrating the strain-tunable LED based on a BP/MoS_2 heterojunction are shown in Figure 3e, where the device is fabricated on a flexible polyimide substrate to apply tensile strain by bending. By transferring BP onto a preannealed polyimide substrate and then rapidly quenching, the mismatch of the coefficient of thermal expansion between BP and the substrate induces built-in compressive strain in BP. Figure 3f presents the variable emission spectra of the BP-LED upon strain applications, exhibiting peak emission wavelength tuning from λ = 4.07 μm (0.20% compressive strain) to λ = 2.70 μm (1.06% tensile strain). The demonstration of an actively and continuously variable-spectrum light source in this spectral region is significant, as this wavelength range consists of various essential bands for optical communications, gas detection, and chemical analysis. A major roadblock in the exploration and realization of tunable mid-IR light sources is the requirement of III−V and II−VI materials prepared by high-cost epitaxial growth and fabrication complexity. Therefore, a variable-spectrum BP-LED provides wide tuning capability equivalent to the integration of numerous devices made from materials with different bandgaps without sacrificing device performance or introducing additional electrical or optical components.

HIGHLY SENSITIVE UNCOOLED MID-IR PHOTODETECTORS

Alongside research focusing on light sources, BP has garnered interest as an active layer for light absorption (photoabsorber), in particular, using bulk BP for mid-IR photodetectors. Its promise as a mid-IR photoabsorber is a result of (i) its strong light absorption at energies above its bulk direct band edge at ~0.3 eV,[20,23] (ii) its high internal quantum efficiency resulting from reduced nonradiative recombination processes,[12] which contributes to a high detectivity figure-of-merit,[13,14] and (iii) its high carrier (hole) mobility, which allows fast device response speeds.[22,58] The position of bulk BP's band edge can also be tuned by the introduction of strain,[59] alloying and doping with other elements such as arsenic ($BP_{1-x}As_x$),[13,60] or layer number,[61] providing tunability in wavelength detection ranges.

To date, most demonstrations of BP photodetectors have utilized two types of device architectures: photoconductors[13,62,63] and photodiodes, as shown in Figure 4a,b, respectively.[14,64−66] The simplest photoconductor structure has two spatially separated electrodes in contact with the BP photoabsorber. When operating, the device is subjected to a fixed bias across the electrodes, with a constant current flowing through the BP channel in the dark (often called dark current), which increases due to the increase in channel conductivity when extra carriers are generated from incident photons. This simple BP photoconductor structure can also exhibit gain in the presence of traps or surface sensitization,[62,67] resulting in detector responsivities much higher than those of their counterpart photodiodes. However, this high responsivity characteristic typically comes at the expense of lower response speeds and a higher noise current, which is an unacceptable trade-off for some applications. Variations on this basic structure include the introduction of top/bottom gates and strategies to enhance the absorption, such as incorporating plasmonic antennas and integrating with optical cavities or waveguides.[58,65,68,69]

The BP photodiode structure requires formation of a *p-n* junction that can separate photoexcited electrons and holes under zero or reverse bias conditions. For BP, the junction can be formed by contacting BP with a different semiconducting material (e.g., a heterojunction with MoS_2)[14,66,70,71] or a metal (a Schottky junction with aluminum).[72] The junction can also be made by locally doping BP electrostatically[64,73,74] or chemically,[75−77] creating a homojunction. Unlike photoconductors, which require a constant bias, photodiodes can operate under zero bias, making them self-powered devices. This benefit scales with the number of pixels in an imager array and is an enabling factor in power-efficient applications. The photodiode structure also has lower noise current in general since a photodiode operates under zero or reverse bias with minimal dark current, as opposed to its photoconductor counterpart that operates with appreciable dark current leading to excessive shot and/or flicker noise. This low operational noise offers the photodiode structure an advantage in achieving a high detectivity.

The specific detectivity D^*, a quantification of the signal-to-noise ratio, is a common photodetector figure-of-merit used to benchmark device performance. A compilation of D^* values at RT from experimental data on BP photodetectors and representative commercially available mid-IR detectors is provided in Figure 4c.[13,14,78−80] The RT D^* values measured on BP and BPAs photodetectors are 6×10^{10} and 2.4×10^{10} cm $Hz^{1/2}$ W^{-1}, rivalling commercial uncooled HgCdTe photodiodes. HgCdTe has been the dominant material system in mid-IR and long-wave-IR in commercial markets, offering high performance devices particularly at low temperature. Nevertheless, even at RT, it is still challenging to find substitutes that achieve a specific detectivity as high as those of HgCdTe photodiodes, typically ~10^{10} cm $Hz^{1/2}$ W^{-1} at wavelengths of 3−4 μm in the mid-IR range (the green solid line in Figure 4c), highlighting the significance of BP as a material system for uncooled IR detectors.

The bandwidth of a photodetector is another critical performance metric. A comparison of BP and BPAs photodetector bandwidths against those of conventional IR photodetectors is included in Figure 4d. While there remains considerable variation in the reported speed of BP-based photodetectors,[14,58,81−83] experimental demonstrations of bandwidths up to GHz frequencies have been achieved,[58] placing them at the upper end of speeds demonstrated by mature commercial photodetectors. The combination of impressive detectivity and bandwidth figures-of-merit demonstrated for BP photodetectors conveys its potential as an outstanding mid-IR photoabsorber.

In addition to these promising figures of merit, BP also exhibits properties allowing novel photodetector functionalities.[14,64,84−86] For example, BP's in-plane anisotropic crystal structure results in strong linear polarization dependent absorption, enabling polarization resolved photodetectors. Figure 4e shows the polarization dependent photoresponse of a BP/MoS_2/BP heterojunction photodiode with two BP absorbers perpendicularly aligned along armchair and zigzag directions, which can be used to extract information about the polarization of incoming light.[14] Similarly, BP IR photodetectors can be incorporated with arbitrary substrates such as

https://doi.org/10.1021/acs.nanolett.4c04027
Nano Lett. 2024, 24, 13107−13117

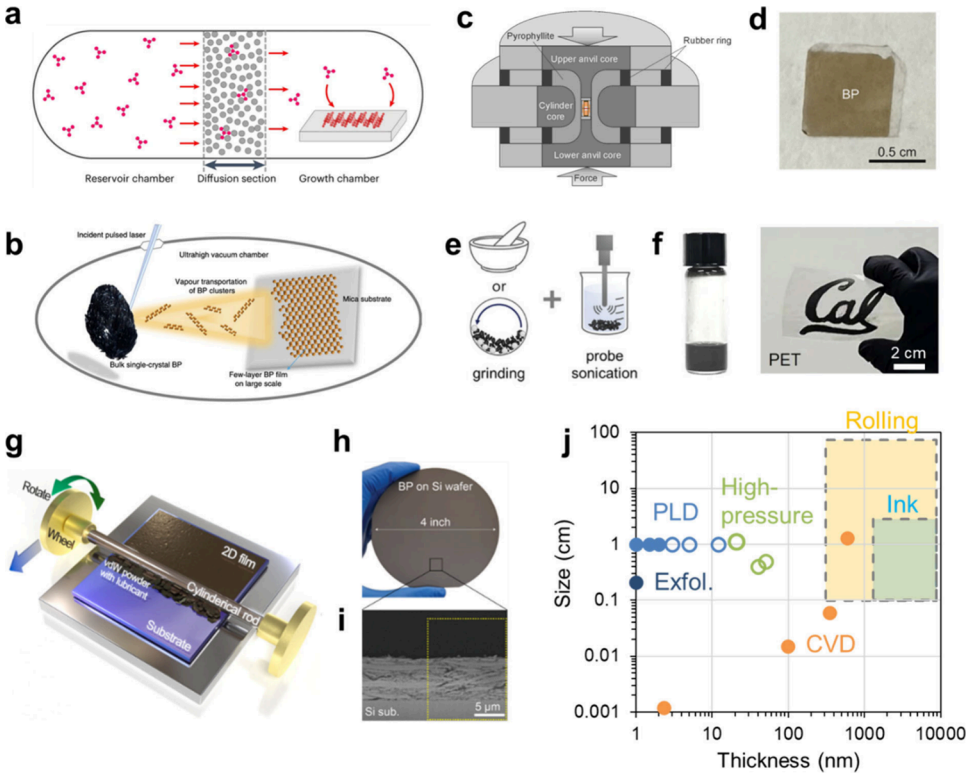

Figure 5. Large-scale processing of BP thin films. (a,b) Schematics of CVD[88] and PLD growth.[89] Reproduced with permission from refs 88 and 89. Copyright 2023 Springer Nature; Copyright 2021 Springer Nature. (c,d) High-pressure conversion of red phosphorus into BP. (c) Schematic of high-pressure apparatus. (d) Centimeter scale BP thin film (18 nm) via high-pressure conversion. Reproduced (adapted) with permission from ref 97. Copyright 2024 American Chemical Society. (e) Ink process for large-scale BP films. Reproduced with permission from ref 99. Copyright 2024 Wiley-VCH. (f) Optical images of BP ink and deposited film on PET substrate. Reproduced with permission from ref 98. Copyright 2023 AAAS. (g–i) Roll printing process. (g) The vdW powders are mixed with lubricant then exfoliated and transferred on the target substrates. (h) Roll-printed BP film on 4 in. Si wafer. (i) Cross-sectional SEM image of BP film. Reproduced (adapted) with permission from ref 100. Copyright 2024 AAAS. (j) Benchmarking of BP film's size and thickness, via mechanical exfoliation (Exfol.),[102] PLD,[89] CVD,[88] High-pressure conversion,[93,94,97] roll-printing,[100] and ink processes.[98,99]

advanced optical structures. For example, the BP photodetectors have been integrated on top of waveguides of various photonic integrated circuit platforms, showing high speed detection, with metalenses showing enhanced absorption, or within Fabry–Perot cavities showing narrow spectral photoresponse.[58,69] Incorporation with flexible substrates has allowed the demonstration of reconfigurable BP photodetectors along with LEDs by introducing lattice strain to BP photodetectors so that the peak spectral photoresponse is blue/red-shifted between λ = 2.44 and 4.32 μm.[15] Another example of reconfigurable devices is a BP spectrometer in which incident light spectra can be reconstructed by a single tunable BP photodetector.[87] The BP detector's spectral photoresponse can be tuned by applying displacement fields to the device. With the help of a learning algorithm, the single BP detector spectrometer can generate a responsivity matrix, based on which the spectrum of the unknown incident light can be reconstructed in the mid-IR range. In addition to reconfigurable devices, bias-selectable multiband photodetectors have been demonstrated with BP.[85] In these studies, BP has been incorporated with other photoabsorbers (e.g., PbS colloidal quantum dots, silicon, and $MoTe_2$) to construct photodetectors whose spectral photoresponse changes based on different bias schemes.

LARGE-SCALE BP THIN FILM AND DEVICE APPLICATIONS

To date, most of the highly efficient BP-based light emitting devices and photodetectors have been based on mechanically exfoliated flakes on the micrometer scale. Scaling up of BP thin films is crucial for the commercialization of these technologies. However, development of a chip-to-wafer scale process has been challenging for BP thin films, unlike other vdW materials such as graphene, *h*-BN, and TMDs. Although BP thin film deposition has been explored by chemical vapor deposition (CVD) (Figure 5a),[88] pulsed laser deposition (PLD) (Figure 5b),[89,90] and molecular beam epitaxy (MBE),[91,92] growth beyond the centimeter scale has been challenging due to difficulties in controlling lateral growth and nucleation sites due to its high surface energies. Specifically, optimized CVD and PLD can provide a chip-scale BP film; however, their growth windows are limited and there are difficulties in controlling thickness.

In contrast to BP, red phosphorus (red-P), another allotrope of phosphorus, is manageable to synthesize into a thin film in a scalable manner via thermal evaporation and PLD.[90,93,94] By utilizing high-pressure treatment, a red-P film can be converted into BP.[93−96] Figure 5c shows a schematic of the high-pressure, high-temperature apparatus for centimeter-scale BP growth. The PLD grown amorphous red-P on mica substrate was successfully converted into a centimeter scale BP thin film (18

https://doi.org/10.1021/acs.nanolett.4c04027
Nano Lett. 2024, 24, 13107−13117

nm thick) by applying 7.7 GPa at RT, as shown in Figure 5d.[97] By optimizing the thermal annealing condition to improve the film quality, the BP film exhibited mid-IR photoemission.[97]

To further scale up BP films, solution-based processes and dry roll-printing methods have been proposed as low-thermal-budget approaches.[98−100] Figure 5e shows a schematic of the BP ink synthesis process: the BP bulk source is ground into microparticles by mortar or ball-mill, then ultrasonicated by a probe sonicator followed by centrifugation to obtain a target BP particle size and thickness distribution.[98,99] Figure 5f shows optical images of the BP ink solution and centimeter-scale deposited film on the target substrate. The film uniformity can be improved by adding a binder such as oleylamine.[98] The peak PL QY of BP ink derived films (PL QY = 0.9%, ∼1.5 μm thick) is comparable to that of exfoliated BP flakes (PL QY = 2.2%, ∼0.6 μm thick). This is attributed to its layered structure that prevents increased nonradiative surface recombination, even in BP particles with a high surface to volume ratio. Notably, BP ink can serve as a "phosphor" when coated onto commercially available visible-wavelength LEDs, enabling a bright emitter converting visible light to mid-IR radiation. The BP ink phosphor emitter achieves an EQE of 0.27%, which is lower than that of LEDs based on exfoliated flakes with optimized optical cavities (EQE = 4.4%).[16,98] To enhance the device performances of the large-scale ink film, further studies are required to optimize the device structure and fabrication process. By adjusting the BP particle size distribution, the emission spectrum was extended from 0.33 eV ($\lambda \approx 3.6$ μm) to 0.80 eV ($\lambda \approx 1.5$ μm), leveraging the quantum confinement effect.[99] The same study showed that $BP_{1-x}As_x$ ink's emission peak shifts to 0.28 eV ($\lambda \approx 4.4$ μm). These scalable, color-tunable BP based ink films can be useful in the realization of mid-IR spectrometers, sensors, and multiplex gas sensing devices.

Figures 5g−i show the dry roll-printing process which can be used to deposit films on a wafer-to-meter scale.[100] This process utilizes sequential exfoliation and transfer of layered materials from powder sources to target substrates through repeated rolling of a cylindrical metal drum. The use of a lubricant, a mixture of octane and mineral oil, facilitates the formation of uniform films. Uniformly coated films were achieved on various mechanically rigid and flexible substrates. The printed films are configured into different devices including LEDs and photodetectors. For the roll-printed BP film, the peak emission wavelength was measured at 0.33 eV, consistent with that of exfoliated BP flakes. Similar to the BP ink film, the PL QY was preserved after the roll-printing process, with a value of 1.6%, comparable to that of tape-exfoliated flakes (PL QY = 2.2%).[100] This technique offers significant benefits in terms of cost-efficiency and a low thermal budget while providing high material quality.[100]

Figure 5j benchmarks different thin film processes. The ink process and roll-printing technique provide large-scale films beyond the wafer scale, unlike other approaches to crystal growth (PLD, CVD) or high-pressure conversion. The active layer thickness is crucial for realizing efficient mid-IR optoelectronic devices; for instance, several tens of nanometers thick layers are optimal for photodetector applications in terms of detectivity.[13,14] Further efforts can be made to control film thickness below 100 nm on a chip-to-wafer scale, utilizing methods such as blade coating and Langmuir−Blodgett deposition techniques.[101]

In summary, BP stands out as a highly promising material for mid-IR optoelectronic applications due to its distinctive optical properties and performance advantages over conventional III−V and II−VI semiconductors. BP's low Auger recombination rate, high quantum efficiency, and inherently self-passivated surface contribute to its superior performance in light-emitting devices and photodetectors. Recent advancements in large-scale thin film processes, such as high-pressure synthesis, solution-based processes, and roll-printing methods, have enabled the fabrication of BP thin films suitable for practical device integration. Despite challenges in stability and scalability, the development of BP-based mid-IR light emitters, including LEDs and lasers, as well as highly sensitive and uncooled photodetectors, highlights its potential for next-generation optoelectronic technologies. Further quantitative time-resolved carrier lifetime measurements will help improve our understanding of photophysics in BP, while future research should focus on optimizing the thin film process and exploring new device architectures to fully harness BP's capabilities in mid-IR applications.

AUTHOR INFORMATION

Corresponding Author

Ali Javey − *Electrical Engineering and Computer Sciences, University of California, Berkeley, Berkeley, California 94720, United States; Materials Sciences Division, Lawrence Berkeley National Laboratory, Berkeley, California 94720, United States; Kavli Energy NanoScience Institute at the University of California, Berkeley, Berkeley, California 94720, United States;* orcid.org/0000-0001-7214-7931; Email: ajavey@berkeley.edu

Authors

Naoki Higashitarumizu − *Electrical Engineering and Computer Sciences, University of California, Berkeley, Berkeley, California 94720, United States; Materials Sciences Division, Lawrence Berkeley National Laboratory, Berkeley, California 94720, United States; JST, PRESTO, Kawaguchi, Saitama 332-0012, Japan;* orcid.org/0000-0003-3996-6753

Shu Wang − *Materials Sciences Division, Lawrence Berkeley National Laboratory, Berkeley, California 94720, United States; Department of Materials Science and Engineering, University of California, Berkeley, Berkeley, California 94720, United States;* orcid.org/0000-0001-8812-817X

Shifan Wang − *Electrical Engineering and Computer Sciences, University of California, Berkeley, Berkeley, California 94720, United States; Materials Sciences Division, Lawrence Berkeley National Laboratory, Berkeley, California 94720, United States; Department of Electrical and Electronic Engineering, University of Melbourne, Melbourne, Victoria 3010, Australia;* orcid.org/0000-0002-9866-1434

Hyungjin Kim − *Department of Materials Science and Engineering, Yonsei University, Seoul 03722, Republic of Korea*

James Bullock − *Department of Electrical and Electronic Engineering, University of Melbourne, Melbourne, Victoria 3010, Australia*

Complete contact information is available at: https://pubs.acs.org/10.1021/acs.nanolett.4c04027

https://doi.org/10.1021/acs.nanolett.4c04027
Nano Lett. 2024, 24, 13107−13117

Author Contributions

The manuscript was written through contributions of all authors.

Author Contributions

N.H., Shu Wang, and and Shifan Wang contributed equally.

Notes

The authors declare no competing financial interest.

■ ACKNOWLEDGMENTS

The work at Berkeley was supported by the U.S. Department of Energy, Office of Science, Office of Basic Energy Sciences, Materials Sciences and Engineering Division, under contract no. DE-AC02-05Ch11231 (Electronic Materials program). N.H. acknowledges support from JST PRESTO (JPMJPR23H7), Japan. J.B. acknowledges support from the Australian Government through the Australian Research Council's Discovery Programs (DP240101309 and DE210101129). H.K. acknowledges support from Samsung Advanced Institute of Technology for part of this research conducted at Yonsei University.

■ REFERENCES

(1) Lambrecht, A.; Schmitt, K. Mid-Infrared Gas-Sensing Systems and Applications. In *Mid-infrared Optoelectronics*; Elsevier: 2020; pp 661−715.

(2) Gordon, I. E.; Rothman, L. S.; Hill, C.; Kochanov, R. V.; Tan, Y.; Bernath, P. F.; Birk, M.; Boudon, V.; Campargue, A.; Chance, K. V.; Drouin, B. J.; Flaud, J.-M.; Gamache, R. R.; Hodges, J. T.; Jacquemart, D.; Perevalov, V. I.; Perrin, A.; Shine, K. P.; Smith, M.-A. H.; Tennyson, J.; Toon, G. C.; Tran, H.; Tyuterev, V. G.; Barbe, A.; Császár, A. G.; Devi, V. M.; Furtenbacher, T.; Harrison, J. J.; Hartmann, J.-M.; Jolly, A.; Johnson, T. J.; Karman, T.; Kleiner, I.; Kyuberis, A. A.; Loos, J.; Lyulin, O. M.; Massie, S. T.; Mikhailenko, S. N.; Moazzen-Ahmadi, N.; Müller, H. S. P.; Naumenko, O. V.; Nikitin, A. V.; Polyansky, O. L.; Rey, M.; Rotger, M.; Sharpe, S. W.; Sung, K.; Starikova, E.; Tashkun, S. A.; Auwera, J. V.; Wagner, G.; Wilzewski, J.; Wcisło, P.; Yu, S.; Zak, E. J. The HITRAN2016 Molecular Spectroscopic Database. *J. Quant. Spectrosc. Radiat. Transfer* **2017**, *203*, 3−69.

(3) Ozaki, Y. Infrared Spectroscopy-Mid-Infrared, near-Infrared, and Far-Infrared/Terahertz Spectroscopy. *Anal. Sci.* **2021**, *37* (9), 1193−1212.

(4) Tamamitsu, M.; Toda, K.; Shimada, H.; Honda, T.; Takarada, M.; Okabe, K.; Nagashima, Y.; Horisaki, R.; Ideguchi, T. Label-Free Biochemical Quantitative Phase Imaging with Mid-Infrared Photothermal Effect. *Optica* **2020**, *7* (4), 359.

(5) Zhao, Y.; Kusama, S.; Furutani, Y.; Huang, W.-H.; Luo, C.-W.; Fuji, T. High-Speed Scanless Entire Bandwidth Mid-Infrared Chemical Imaging. *Nat. Commun.* **2023**, *14* (1), 3929.

(6) Gade, R.; Moeslund, T. B. Thermal Cameras and Applications: A Survey. *Mach. Vis. Appl.* **2014**, *25* (1), 245−262.

(7) Dam, J. S.; Tidemand-Lichtenberg, P.; Pedersen, C. Room-Temperature Mid-Infrared Single-Photon Spectral Imaging. *Nat. Photonics* **2012**, *6* (11), 788−793.

(8) Zhang, H.; Prado, Y.; Alchaar, R.; Lehouelleur, H.; Cavallo, M.; Dang, T. H.; Khalili, A.; Bossavit, E.; Dabard, C.; Ledos, N.; Silly, M. G; Madouri, A.; Fournier, D.; Utterback, J. K.; Pierucci, D.; Parahyba, V.; Potet, P.; Darson, D.; Ithurria, S.; Bartlomiej Szafran; Diroll, B. T.; Climente, J. I.; Lhuillier, E. Infrared Imaging Using Thermally Stable HgTe/CdS Nanocrystals. *Nano Lett.* **2024**, *24* (16), 5039−5046.

(9) A. Gaus, Y. F.; Bhowmik, N.; Isaac-Medina, B. K.; Breckon, T. P. Visible to Infrared Transfer Learning as a Paradigm for Accessible Real-Time Object Detection and Classification in Infrared Imagery. In *Counterterrorism, Crime Fighting, Forensics, and Surveillance Technologies IV*; Bouma, H., Stokes, R. J., Yitzhaky, Y., Prabhu, R., Eds.; SPIE: 2020; Vol. *11542*, pp 13−27.

(10) Swanson, R. M. A Proposed Thermophotovoltaic Solar Energy Conversion System. *Proc. IEEE Inst. Electr. Electron. Eng.* **1979**, *67* (3), 446−447.

(11) LaPotin, A.; Schulte, K. L.; Steiner, M. A.; Buznitsky, K.; Kelsall, C. C.; Friedman, D. J.; Tervo, E. J.; France, R. M.; Young, M. R.; Rohskopf, A.; Verma, S.; Wang, E. N.; Henry, A. Thermophotovoltaic Efficiency of 40. *Nature* **2022**, *604* (7905), 287−291.

(12) Higashitarumizu, N.; Uddin, S. Z.; Weinberg, D.; Azar, N. S.; Reaz Rahman, I. K. M.; Wang, V.; Crozier, K. B.; Rabani, E.; Javey, A. Anomalous Thickness Dependence of Photoluminescence Quantum Yield in Black Phosphorous. *Nat. Nanotechnol.* **2023**, *18* (5), 507−513.

(13) Amani, M.; Regan, E.; Bullock, J.; Ahn, G. H.; Javey, A. Mid-Wave Infrared Photoconductors Based on Black Phosphorus-Arsenic Alloys. *ACS Nano* **2017**, *11* (11), 11724−11731.

(14) Bullock, J.; Amani, M.; Cho, J.; Chen, Y.-Z.; Ahn, G. H.; Adinolfi, V.; Shrestha, V. R.; Gao, Y.; Crozier, K. B.; Chueh, Y.-L.; Javey, A. Polarization-Resolved Black Phosphorus/Molybdenum Disulfide Mid-Wave Infrared Photodiodes with High Detectivity at Room Temperature. *Nat. Photonics* **2018**, *12* (10), 601−607.

(15) Kim, H.; Uddin, S. Z.; Lien, D.-H.; Yeh, M.; Azar, N. S.; Balendhran, S.; Kim, T.; Gupta, N.; Rho, Y.; Grigoropoulos, C. P.; Crozier, K. B.; Javey, A. Actively Variable-Spectrum Optoelectronics with Black Phosphorus. *Nature* **2021**, *596* (7871), 232−237.

(16) Gupta, N.; Kim, H.; Azar, N. S.; Uddin, S. Z.; Lien, D.-H.; Crozier, K. B.; Javey, A. Bright Mid-Wave Infrared Resonant-Cavity Light-Emitting Diodes Based on Black Phosphorus. *Nano Lett.* **2022**, *22* (3), 1294−1301.

(17) Higashitarumizu, N.; Tajima, S.; Kim, J.; Cai, M.; Javey, A. Long Operating Lifetime Mid-Infrared LEDs Based on Black Phosphorus. *Nat. Commun.* **2023**, *14* (1), 4845.

(18) Zhang, Y.; Wang, S.; Chen, S.; Zhang, Q.; Wang, X.; Zhu, X.; Zhang, X.; Xu, X.; Yang, T.; He, M.; Yang, X.; Li, Z.; Chen, X.; Wu, M.; Lu, Y.; Ma, R.; Lu, W.; Pan, A. Wavelength-Tunable Mid-Infrared Lasing from Black Phosphorus Nanosheets. *Adv. Mater.* **2020**, *32* (17), No. e1808319.

(19) Chen, C.; Chen, F.; Chen, X.; Deng, B.; Eng, B.; Jung, D.; Guo, Q.; Yuan, S.; Watanabe, K.; Taniguchi, T.; Lee, M. L.; Xia, F. Bright Mid-Infrared Photoluminescence from Thin-Film Black Phosphorus. *Nano Lett.* **2019**, *19* (3), 1488−1493.

(20) Low, T.; Rodin, A. S.; Carvalho, A.; Jiang, Y.; Wang, H.; Xia, F.; Castro Neto, A. H. Tunable Optical Properties of Multilayer Black Phosphorus Thin Films. *Phys. Rev. B Condens. Matter Mater. Phys.* **2014**, *90* (7), 075434.

(21) Ling, X.; Wang, H.; Huang, S.; Xia, F.; Dresselhaus, M. S. The Renaissance of Black Phosphorus. *Proc. Natl. Acad. Sci. U. S. A.* **2015**, *112* (15), 4523−4530.

(22) Qiao, J.; Kong, X.; Hu, Z.-X.; Yang, F.; Ji, W. High-Mobility Transport Anisotropy and Linear Dichroism in Few-Layer Black Phosphorus. *Nat. Commun.* **2014**, *5* (1), 4475.

(23) Li, L.; Yu, Y.; Ye, G. J.; Ge, Q.; Ou, X.; Wu, H.; Feng, D.; Chen, X. H.; Zhang, Y. Black Phosphorus Field-Effect Transistors. *Nat. Nanotechnol.* **2014**, *9* (5), 372−377.

(24) Yoo, S. J.; Kim, H.; Lee, J.-H.; Kim, J.-G. Direct Observation of Thermal Disorder and Decomposition of Black Phosphorus. *Nanotechnology* **2018**, *29* (6), 065702.

(25) Blundo, E.; Felici, M.; Yildirim, T.; Pettinari, G.; Tedeschi, D.; Miriametro, A.; Liu, B.; Ma, W.; Lu, Y.; Polimeni, A. Evidence of the Direct-to-Indirect Band Gap Transition in Strained Two-Dimensional WS_2, MoS_2, and WSe_2. *Phys. Rev. Res.* **2020**, *2* (1), 012024.

(26) Lezama, I. G.; Arora, A.; Ubaldini, A.; Barreteau, C.; Giannini, E.; Potemski, M.; Morpurgo, A. F. Indirect-to-Direct Band Gap Crossover in Few-Layer $MoTe_2$. *Nano Lett.* **2015**, *15* (4), 2336−2342.

(27) Amani, M.; Lien, D.-H.; Kiriya, D.; Xiao, J.; Azcatl, A.; Noh, J.; Madhvapathy, S. R.; Addou, R.; Kc, S.; Dubey, M.; Cho, K.; Wallace, R. M.; Lee, S.-C.; He, J.-H.; Ager, J. W., 3rd; Zhang, X.; Yablonovitch, E.; Javey, A. Near-Unity Photoluminescence Quantum Yield in MoS_2. *Science* **2015**, *350* (6264), 1065−1068.

https://doi.org/10.1021/acs.nanolett.4c04027
Nano Lett. 2024, 24, 13107−13117

(28) Lien, D.-H.; Uddin, S. Z.; Yeh, M.; Amani, M.; Kim, H.; Ager, J. W., 3rd; Yablonovitch, E.; Javey, A. Electrical Suppression of All Nonradiative Recombination Pathways in Monolayer Semiconductors. *Science* **2019**, *364* (6439), 468−471.
(29) Kim, H.; Uddin, S. Z.; Higashitarumizu, N.; Rabani, E.; Javey, A. Inhibited Nonradiative Decay at All Exciton Densities in Monolayer Semiconductors. *Science* **2021**, *373* (6553), 448−452.
(30) Wang, H.; Zhang, C.; Rana, F. Ultrafast Dynamics of Defect-Assisted Electron-Hole Recombination in Monolayer MoS_2. *Nano Lett.* **2015**, *15* (1), 339−345.
(31) Hall, R. N. Electron-Hole Recombination in Germanium. In *Semiconductor Devices: Pioneering Papers*; WORLD SCIENTIFIC: 1991; pp 70−70.
(32) Shockley, W.; Read, W. T. Statistics of the Recombinations of Holes and Electrons. *Phys. Rev.* **1952**, *87* (5), 835−842.
(33) McIntosh, K. R.; Black, L. E. On Effective Surface Recombination Parameters. *J. Appl. Phys.* **2014**, *116* (1), 014503.
(34) Haug, A. Auger Recombination in Direct-Gap Semiconductors: Band-Structure Effects. *J. phys.* **1983**, *16* (21), 4159−4172.
(35) Bhaskar, P.; Achtstein, A. W.; Vermeulen, M. J. W.; Siebbeles, L. D. A. Radiatively Dominated Charge Carrier Recombination in Black Phosphorus. *J. Phys. Chem. C* **2016**, *120* (25), 13836−13842.
(36) Suess, R. J.; Leong, E.; Garrett, J. L.; Zhou, T.; Salem, R.; Munday, J. N.; Murphy, T. E.; Mittendorff, M. Mid-Infrared Time-Resolved Photoconduction in Black Phosphorus. *2d Mater.* **2016**, *3* (4), 041006.
(37) Aytac, Y.; Mittendorff, M.; Murphy, T. E. Probing the Free-Carrier Absorption in Multi-Layer Black Phosphorus. *Appl. Phys. Lett.* **2018**, *113* (3), 031108.
(38) Edmonds, M. T.; Tadich, A.; Carvalho, A.; Ziletti, A.; O'Donnell, K. M.; Koenig, S. P.; Coker, D. F.; Özyilmaz, B.; Neto, A. H. C.; Fuhrer, M. S. Creating a Stable Oxide at the Surface of Black Phosphorus. *ACS Appl. Mater. Interfaces* **2015**, *7* (27), 14557−14562.
(39) Zhou, Q.; Chen, Q.; Tong, Y.; Wang, J. Light-Induced Ambient Degradation of Few-Layer Black Phosphorus: Mechanism and Protection. *Angew. Chem., Int. Ed. Engl.* **2016**, *55* (38), 11437−11441.
(40) Luo, W.; Zemlyanov, D. Y.; Milligan, C. A.; Du, Y.; Yang, L.; Wu, Y.; Ye, P. D. Surface Chemistry of Black Phosphorus under a Controlled Oxidative Environment. *Nanotechnology* **2016**, *27* (43), 434002.
(41) Ziletti, A.; Carvalho, A.; Trevisanutto, P. E.; Campbell, D. K.; Coker, D. F.; Castro Neto, A. H. Phosphorene Oxides: Bandgap Engineering of Phosphorene by Oxidation. *Phys. Rev. B Condens. Matter Mater. Phys.* **2015**, *91* (8), 085407.
(42) Wood, J. D.; Wells, S. A.; Jariwala, D.; Chen, K.-S.; Cho, E.; Sangwan, V. K.; Liu, X.; Lauhon, L. J.; Marks, T. J.; Hersam, M. C. Effective Passivation of Exfoliated Black Phosphorus Transistors against Ambient Degradation. *Nano Lett.* **2014**, *14* (12), 6964−6970.
(43) Ziletti, A.; Carvalho, A.; Campbell, D. K.; Coker, D. F.; Castro Neto, A. H. Oxygen Defects in Phosphorene. *Phys. Rev. Lett.* **2015**, *114* (4), 046801.
(44) Faist, J.; Capasso, F.; Sivco, D. L.; Sirtori, C.; Hutchinson, A. L.; Cho, A. Y. Quantum Cascade Laser. *Science* **1994**, *264* (5158), 553−556.
(45) Yao, Y.; Hoffman, A. J.; Gmachl, C. F. Mid-Infrared Quantum Cascade Lasers. *Nat. Photonics* **2012**, *6* (7), 432−439.
(46) Kurtz, S. R.; Biefeld, R. M.; Dawson, L. R. Modification of Valence-Band Symmetry and Auger Threshold Energy in Biaxially Compressed $InAs_{1-x}Sb_x$. *Phys. Rev. B Condens. Matter* **1995**, *51* (11), 7310−7313.
(47) Kinch, M. A.; Brau, M. J.; Simmons, A. Recombination Mechanisms in 8−14-μ HgCdTe. *J. Appl. Phys.* **1973**, *44* (4), 1649−1663.
(48) Popov, A. A.; Stepanov, M. V.; Sherstnev, V. V.; Yakovlev, Y. P. 3.3-Mm LEDs for Measuring Methane. *Technol. Phys. Lett.* **1997**, *23* (11), 828−830.
(49) Hadji, E.; Bleuse, J.; Magnea, N.; Pautrat, J. L. 3.2 Mm Infrared Resonant Cavity Light Emitting Diode. *Appl. Phys. Lett.* **1995**, *67* (18), 2591−2593.
(50) Das, N. C.; Olver, K.; Towner, F.; Simonis, G.; Shen, H. Infrared (3.8μm) Interband Cascade Light-Emitting Diode Array with Record High Efficiency. *Appl. Phys. Lett.* **2005**, *87* (4), 041105.
(51) Das, N. C. Infrared Light Emitting Device with Two Color Emission. *Solid-State Electron.* **2010**, *54* (11), 1381−1383.
(52) Bandyopadhyay, N.; Slivken, S.; Bai, Y.; Razeghi, M. High Power, Continuous Wave, Room Temperature Operation of $\lambda \sim 3.4$ Mm and $\lambda \sim 3.55$ Mm InP-Based Quantum Cascade Lasers. *Appl. Phys. Lett.* **2012**, *100* (21), 212104.
(53) Xie, F.; Caneau, C.; LeBlanc, H. P.; Visovsky, N. J.; Chaparala, S. C.; Deichmann, O. D.; Hughes, L. C.; Zah, C.-E.; Caffey, D. P.; Day, T. Room Temperature CW Operation of Short Wavelength Quantum Cascade Lasers Made of Strain Balanced $Ga_xIn_{1-x}As$/$Al_yIn_{1-y}As$ Material on InP Substrates. *IEEE J. Sel. Top. Quantum Electron.* **2011**, *17* (5), 1445−1452.
(54) Popov, A. A.; Stepanov, M. V.; Sherstnev, V. V.; Yakovlev, Y. P. InAsSb Light-Emitting Diodes for the Detection of CO_2 ($\lambda = 4.3$ μm). *Technical Physics Letters* **1998**, *24* (8), 596−598.
(55) Popov, A. A.; Sherstnev, V. V.; Yakovlev, Y. P. Light-Emitting Diodes for the 1.7−2.4 μm Wavelengths. In *Light-Emitting Diodes: Research, Manufacturing, and Applications*; SPIE: 1997; Vol. *3002*, pp 132−140.
(56) Huang, S.; Zhang, G.; Fan, F.; Song, C.; Wang, F.; Xing, Q.; Wang, C.; Wu, H.; Yan, H. Strain-Tunable van Der Waals Interactions in Few-Layer Black Phosphorus. *Nat. Commun.* **2019**, *10* (1), 2447.
(57) Ma, W.; Lu, J.; Wan, B.; Peng, D.; Xu, Q.; Hu, G.; Peng, Y.; Pan, C.; Wang, Z. L. Piezoelectricity in Multilayer Black Phosphorus for Piezotronics and Nanogenerators. *Adv. Mater.* **2020**, *32* (7), No. e1905795.
(58) Youngblood, N.; Chen, C.; Koester, S. J.; Li, M. Waveguide-Integrated Black Phosphorus Photodetector with High Responsivity and Low Dark Current. *Nat. Photonics* **2015**, *9* (4), 247−252.
(59) Rodin, A. S.; Carvalho, A.; Castro Neto, A. H. Strain-Induced Gap Modification in Black Phosphorus. *Phys. Rev. Lett.* **2014**, *112* (17), 176801.
(60) Wang, S.; Higashitarumizu, N.; Sari, B.; Scott, M. C.; Javey, A. Quantitative Mid-Infrared Photoluminescence Characterization of Black Phosphorus-Arsenic Alloys. *ACS Nano* **2024**, *18* (7), 5219−5994.
(61) Tran, V.; Soklaski, R.; Liang, Y.; Yang, L. Layer-Controlled Band Gap and Anisotropic Excitons in Few-Layer Black Phosphorus. *Phys. Rev. B Condens. Matter Mater. Phys.* **2014**, *89* (23), 235319.
(62) Guo, Q.; Pospischil, A.; Bhuiyan, M.; Jiang, H.; Tian, H.; Farmer, D.; Deng, B.; Li, C.; Han, S.-J.; Wang, H.; Xia, Q.; Ma, T.-P.; Mueller, T.; Xia, F. Black Phosphorus Mid-Infrared Photodetectors with High Gain. *Nano Lett.* **2016**, *16* (7), 4648−4655.
(63) Yuan, S.; Shen, C.; Deng, B.; Chen, X.; Guo, Q.; Ma, Y.; Abbas, A.; Liu, B.; Haiges, R.; Ott, C.; Nilges, T.; Watanabe, K.; Taniguchi, T.; Sinai, O.; Naveh, D.; Zhou, C.; Xia, F. Air-Stable Room-Temperature Mid-Infrared Photodetectors Based on hBN/Black Arsenic Phosphorus/hBN Heterostructures. *Nano Lett.* **2018**, *18* (5), 3172−3179.
(64) Yuan, H.; Liu, X.; Afshinmanesh, F.; Li, W.; Xu, G.; Sun, J.; Lian, B.; Curto, A. G.; Ye, G.; Hikita, Y.; Shen, Z.; Zhang, S.-C.; Chen, X.; Brongersma, M.; Hwang, H. Y.; Cui, Y. Polarization-Sensitive Broadband Photodetector Using a Black Phosphorus Vertical *p-n* Junction. *Nat. Nanotechnol.* **2015**, *10* (8), 707−713.
(65) Yan, W.; Shresha, V. R.; Jeangros, Q.; Azar, N. S.; Balendhran, S.; Ballif, C.; Crozier, K.; Bullock, J. Spectrally Selective Mid-Wave Infrared Detection Using Fabry-Pérot Cavity Enhanced Black Phosphorus 2D Photodiodes. *ACS Nano* **2020**, *14* (10), 13645−13651.
(66) Deng, Y.; Luo, Z.; Conrad, N. J.; Liu, H.; Gong, Y.; Najmaei, S.; Ajayan, P. M.; Lou, J.; Xu, X.; Ye, P. D. Black Phosphorus-Monolayer MoS_2 van Der Waals Heterojunction *p-n* Diode. *ACS Nano* **2014**, *8* (8), 8292−8299.
(67) Engel, M.; Steiner, M.; Avouris, P. Black Phosphorus Photodetector for Multispectral, High-Resolution Imaging. *Nano Lett.* **2014**, *14* (11), 6414−6417.

https://doi.org/10.1021/acs.nanolett.4c04027
Nano Lett. 2024, 24, 13107−13117

(68) Venuthurumilli, P. K.; Ye, P. D.; Xu, X. Plasmonic Resonance Enhanced Polarization-Sensitive Photodetection by Black Phosphorus in near Infrared. *ACS Nano* **2018**, *12* (5), 4861−4867.
(69) Wang, S.; Chapman, R. J.; Johnson, B. C.; Krasnokutska, I.; Tambasco, J.-L. J.; Messalea, K.; Peruzzo, A.; Bullock, J. Integration of Black Phosphorus Photoconductors with Lithium Niobate on Insulator Photonics. *Adv. Opt. Mater.* **2023**, *11* (2), 2201688.
(70) Chen, P.; Zhang, T. T.; Zhang, J.; Xiang, J.; Yu, H.; Wu, S.; Lu, X.; Wang, G.; Wen, F.; Liu, Z.; Yang, R.; Shi, D.; Zhang, G. Gate Tunable WSe_2-BP van Der Waals Heterojunction Devices. *Nanoscale* **2016**, *8* (6), 3254−3258.
(71) Shim, J.; Oh, S.; Kang, D.-H.; Jo, S.-H.; Ali, M. H.; Choi, W.-Y.; Heo, K.; Jeon, J.; Lee, S.; Kim, M.; Song, Y. J.; Park, J.-H. Phosphorene/Rhenium Disulfide Heterojunction-Based Negative Differential Resistance Device for Multi-Valued Logic. *Nat. Commun.* **2016**, *7* (1), 13413.
(72) Miao, J.; Zhang, S.; Cai, L.; Wang, C. Black Phosphorus Schottky Diodes: Channel Length Scaling and Application as Photodetectors. *Adv. Electron. Mater.* **2016**, *2* (4), 1500346.
(73) Buscema, M.; Groenendijk, D. J.; Steele, G. A.; van der Zant, H. S. J.; Castellanos-Gomez, A. Photovoltaic Effect in Few-Layer Black Phosphorus PN Junctions Defined by Local Electrostatic Gating. *Nat. Commun.* **2014**, *5* (1), 4651.
(74) Yan, W.; Wang, S.; Xing, K.; Balendhran, S.; Tebyetekerwa, M.; Watanabe, K.; Taniguchi, T.; Fuhrer, M. S.; Crozier, K. B.; Bullock, J. Electrostatically Induced Black Phosphorus Infrared Photodiodes. *Adv. Funct. Mater.* **2024**, *34* (32), 2316000.
(75) Liu, Y.; Cai, Y.; Zhang, G.; Zhang, Y.-W.; Ang, K.-W. Al-doped Black Phosphorus *p-n* Homojunction Diode for High Performance Photovoltaic. *Adv. Funct. Mater.* **2017**, *27* (7), 1604638.
(76) Xu, Y.; Liu, C.; Guo, C.; Yu, Q.; Guo, W.; Lu, W.; Chen, X.; Wang, L.; Zhang, K. High Performance near Infrared Photodetector Based on In-Plane Black Phosphorus *p-n* Homojunction. *Nano Energy* **2020**, *70*, 104518.
(77) Kim, D.-K.; Hong, S.-B.; Jeong, K.; Lee, C.; Kim, H.; Cho, M.-H. P-N Junction Diode Using Plasma Boron-Doped Black Phosphorus for High-Performance Photovoltaic Devices. *ACS Nano* **2019**, *13* (2), 1683−1693.
(78) Xue, X.; Chen, M.; Luo, Y.; Qin, T.; Tang, X.; Hao, Q. High-Operating-Temperature Mid-Infrared Photodetectors via Quantum Dot Gradient Homojunction. *Light Sci. Appl.* **2023**, *12* (1), 2.
(79) *High sensitivity infrared detectors and detection solutions*. VIGO Photonics USA. https://vigophotonics.com/us/products/infrared-detectors/ (accessed 2024-07-02).
(80) Rogalski, A.; Martyniuk, P.; Kopytko, M.; Hu, W. Trends in Performance Limits of the HOT Infrared Photodetectors. *Appl. Sci.* **2021**, *11* (2), 501.
(81) Youngblood, N.; Li, M. Ultrafast Photocurrent Measurements of a Black Phosphorus Photodetector. *Appl. Phys. Lett.* **2017**, *110* (5), 051102.
(82) Chang, T.-Y.; Chen, P.-L.; Yan, J.-H.; Li, W.-Q.; Zhang, Y.-Y.; Luo, D.-I.; Li, J.-X.; Huang, K.-P.; Liu, C.-H. Ultra-Broadband, High Speed, and High-Quantum-Efficiency Photodetectors Based on Black Phosphorus. *ACS Appl. Mater. Interfaces* **2020**, *12* (1), 1201−1209.
(83) Ye, L.; Li, H.; Chen, Z.; Xu, J. Near-Infrared Photodetector Based on MoS_2/Black Phosphorus Heterojunction. *ACS Photonics* **2016**, *3* (4), 692−699.
(84) Wu, S.; Chen, Y.; Wang, X.; Jiao, H.; Zhao, Q.; Huang, X.; Tai, X.; Zhou, Y.; Chen, H.; Wang, X.; Huang, S.; Yan, H.; Lin, T.; Shen, H.; Hu, W.; Meng, X.; Chu, J.; Wang, J. Ultra-Sensitive Polarization-Resolved Black Phosphorus Homojunction Photodetector Defined by Ferroelectric Domains. *Nat. Commun.* **2022**, *13* (1), 3198.
(85) Wang, S.; Ashokan, A.; Balendhran, S.; Yan, W.; Johnson, B. C.; Peruzzo, A.; Crozier, K. B.; Mulvaney, P.; Bullock, J. Room Temperature Bias-Selectable, Dual-Band Infrared Detectors Based on Lead Sulfide Colloidal Quantum Dots and Black Phosphorus. *ACS Nano* **2023**, *17* (12), 11771−11782.
(86) Wu, P.; Ye, L.; Tong, L.; Wang, P.; Wang, Y.; Wang, H.; Ge, H.; Wang, Z.; Gu, Y.; Zhang, K.; Yu, Y.; Peng, M.; Wang, F.; Huang, M.; Zhou, P.; Hu, W. Van Der Waals Two-Color Infrared Photodetector. *Light Sci. Appl.* **2022**, *11* (1), 6.
(87) Yuan, S.; Naveh, D.; Watanabe, K.; Taniguchi, T.; Xia, F. A Wavelength-Scale Black Phosphorus Spectrometer. *Nat. Photonics* **2021**, *15* (8), 601−607.
(88) Chen, C.; Yin, Y.; Zhang, R.; Yuan, Q.; Xu, Y.; Zhang, Y.; Chen, J.; Zhang, Y.; Li, C.; Wang, J.; Li, J.; Fei, L.; Yu, Q.; Zhou, Z.; Zhang, H.; Cheng, R.; Dong, Z.; Xu, X.; Pan, A.; Zhang, K.; He, J. Growth of Single-Crystal Black Phosphorus and Its Alloy Films through Sustained Feedstock Release. *Nat. Mater.* **2023**, *22* (6), 717−724.
(89) Wu, Z.; Lyu, Y.; Zhang, Y.; Ding, R.; Zheng, B.; Yang, Z.; Lau, S. P.; Chen, X. H.; Hao, J. Large-Scale Growth of Few-Layer Two-Dimensional Black Phosphorus. *Nat. Mater.* **2021**, *20* (9), 1203−1209.
(90) Yang, Z.; Hao, J.; Yuan, S.; Lin, S.; Yau, H. M.; Dai, J.; Lau, S. P. Field-Effect Transistors Based on Amorphous Black Phosphorus Ultrathin Films by Pulsed Laser Deposition. *Adv. Mater.* **2015**, *27* (25), 3748−3754.
(91) Xu, H.; Han, X.; Li, Z.; Liu, W.; Li, X.; Wu, J.; Guo, Z.; Liu, H. Epitaxial Growth of Few-layer Black Phosphorene Quantum Dots on Si Substrates. *Adv. Mater. Interfaces* **2018**, *5* (21), 1801048.
(92) Zhu, Y.; Cao, J.; Liu, S.; Loh, K. P. Heteroepitaxial Growth of Black Phosphorus on Tin Monosulfide. *Nano Lett.* **2024**, *24* (1), 479−485.
(93) Li, X.; Deng, B.; Wang, X.; Chen, S.; Vaisman, M.; Karato, S.-I.; Pan, G.; Lee, M. L.; Cha, J.; Wang, H.; Xia, F. Synthesis of Thin-Film Black Phosphorus on a Flexible Substrate. *2D Mater.* **2015**, *2* (3), 031002.
(94) Li, C.; Wu, Y.; Deng, B.; Xie, Y.; Guo, Q.; Yuan, S.; Chen, X.; Bhuiyan, M.; Wu, Z.; Watanabe, K.; Taniguchi, T.; Wang, H.; Cha, J. J.; Snure, M.; Fei, Y.; Xia, F. Synthesis of Crystalline Black Phosphorus Thin Film on Sapphire. *Adv. Mater.* **2018**, *30* (6), 1703748.
(95) Rissi, E. N.; Soignard, E.; McKiernan, K. A.; Benmore, C. J.; Yarger, J. L. Pressure-Induced Crystallization of Amorphous Red Phosphorus. *Solid State Commun.* **2012**, *152* (5), 390−394.
(96) Endo, S.; Akahama, Y.; Terada, S.-I.; Narita, S.-I. Growth of Large Single Crystals of Black Phosphorus under High Pressure. *Jpn. J. Appl. Phys.* **1982**, *21* (8A), L482.
(97) Higashitarumizu, N.; Kawashima, T.; Smart, T.; Yalisove, R.; Ho, C. Y.; Madsen, M.; Chrzan, D. C.; Scott, M. C.; Jeanloz, R.; Yusa, H.; Javey, A. Mid-Infrared, Optically Active Black Phosphorus Thin Films on Centimeter Scale. *Nano Lett.* **2024**, *24* (10), 3104−3111.
(98) Gupta, N.; Wang, S.; Higashitarumizu, N.; Wang, V.; Lee, K.; Park, C.; Javey, A. Large-Scale Efficient Mid-Wave Infrared Optoelectronics Based on Black Phosphorus Ink. *Sci. Adv.* **2023**, *9* (49), No. eadi9384.
(99) Kim, J. I.; Higashitarumizu, N.; Wang, S.; Yalisove, R.; Scott, M. C.; Song, S. Y.; Javey, A. Multicolor Inks of Black Phosphorus for Midwave-Infrared Optoelectronics. *Adv. Mater.* **2024**, *36* (30), No. e2402922.
(100) Lee, K.; Higashitarumizu, N.; Wang, S.; Kim, C.; Ho, C. Y.; Oh, J. W.; Zan, G.; Madsen, M.; Lee, T.-W.; Chrzan, D. C.; Park, C.; Javey, A. Meter-Scale van Der Waals Films Manufactured via One-Step Roll Printing. *Sci. Adv.* **2024**, *10* (36), No. eadq0655.
(101) Xu, L.; Tetreault, A. R.; Khaligh, H. H.; Goldthorpe, I. A.; Wettig, S. D.; Pope, M. A. Continuous Langmuir-Blodgett Deposition and Transfer by Controlled Edge-to-Edge Assembly of Floating 2D Materials. *Langmuir* **2019**, *35* (1), 51−59.
(102) Huang, Y.; Pan, Y.-H.; Yang, R.; Bao, L.-H.; Meng, L.; Luo, H.-L.; Cai, Y.-Q.; Liu, G.-D.; Zhao, W.-J.; Zhou, Z.; Wu, L.-M.; Zhu, Z.-L.; Huang, M.; Liu, L.-W.; Liu, L.; Cheng, P.; Wu, K.-H.; Tian, S.-B.; Gu, C.-Z.; Shi, Y.-G.; Guo, Y.-F.; Cheng, Z. G.; Hu, J.-P.; Zhao, L.; Yang, G.-H.; Sutter, E.; Sutter, P.; Wang, Y.-L.; Ji, W.; Zhou, X.-J.; Gao, H.-J. Universal Mechanical Exfoliation of Large-Area 2D Crystals. *Nat. Commun.* **2020**, *11* (1), 2453.

https://doi.org/10.1021/acs.nanolett.4c04027
Nano Lett. 2024, 24, 13107−13117